A Crystalline/Amorphous Cobalt(II,III) Oxide Hybrid Electrocatalyst for Lithium–Air Batteries

S. Mohammad B. Khajehbashi,[a] Jiantao Li,[a] Manman Wang,[a] Lin Xu,[a, b] Kangning Zhao,[a] Qiulong Wei,[a] Changwei Shi,[a] Chunjuan Tang,[a] Lei Huang,[a] Zhaoyang Wang,[a] and Liqiang Mai*[a]

Weakening of the oxygen bond is the main intention in the design and synthesis of catalysts for the oxygen reduction reaction (ORR). Hybrid-structured electrocatalysts are promising candidates for this purpose; however, the use of noble metals and the combination of different materials, such as graphene and metal oxides, usually limits their synthesis on the laboratory scale. Herein, we introduce an oxidation and rapid-cooling process as a novel and facile way to synthesize a bare Co_3O_4 hybrid crystalline/amorphous catalyst. Characterization of this material shows that the facile synthesis process is effective in forming an amorphous layer on the crystal structure of Co_3O_4. The cyclic voltammetry and rotating disc electrode results in aqueous solution prove the good performance of the catalyst. A Li–air battery with this catalyst successfully sustains about 2500 h of continuous cycling (120 cycles) with an average discharge voltage of 2.80 V and a limited specific capacity of 1000 mAh g^{-1}, which proves the high performance of this catalyst in non-aqueous electrolyte. We show that the origin of the high catalytic performance in this hybrid structure derives from the synergistic behavior of two different active sites, and this concept facilitates the design and synthesis of electrocatalysts by rapid-cooling synthesis for the industrial scale.

Introduction

Li–air batteries with high theoretical specific energy density are attracting more attention for practical use in electrical vehicles. Processes in these batteries include the oxygen reduction reaction (ORR) and the oxygen evolution reaction (OER). Because of these reactions, the theoretical energy density of Li–air batteries can reach a value almost as high as that of gasoline; however, until now the practical use of Li–air batteries has not gained momentum, and there are fundamental questions behind the way in which they function.[1–15] The pores in the cathode of a Li–air battery can be blocked by products from the ORR. In addition, the high activation polarization of the ORR cannot be ignored and sluggish kinetics of the ORR/OER decrease the energy conversion efficiency.[4,8,16–19] According to many researchers, the use of catalysts is definitely a way to reduce the reaction barrier and to facilitate the reaction kinetics.[16–28] Catalysts not only reduce the overpotential of the reaction by reducing the needed activation energy, but they also determine the size and distribution of the lithium oxides by providing nucleation regions.

Recently, precious metals or a combination of different materials such as metal oxides and graphene oxide have been used to synthesize hybrid catalysts.[16,17,20,24,29,30] Liang et al. proved that Co_3O_4 or graphene oxide alone has little catalytic activity for the ORR but that the Co_3O_4–graphene oxide hybrid material exhibits high activity in the ORR in alkaline solutions.[17] In other work, they showed the CoO/carbon nanotube (CNT) hybrid structure has high performance in terms of charge transport and active catalytic sites. They believe the CoO/CNT hybrid is a promising alternative to Pt for the ORR under alkaline conditions.[18] As mentioned, cobalt oxides in hierarchical structures or supported with graphene oxide, CNTs, and some other metal oxides have been employed as catalysts in the ORR or metal–air batteries.[3,11,17,18,24,31–33]

Herein, we introduce a unique method to synthesize a hybrid catalyst, only by use of bare Co_3O_4 nanoparticles. By this strategy, the in situ hybrid Co_3O_4 nanoparticles without any supporting material or hierarchical structure can provide high catalytic performance. Amorphous catalysts are considered as high-performance catalysts in competition with crystalline catalysts.[3,16,19,34] The rapid-cooling method to synthesize an amorphous structure in a bulk material and the use of this hypothesis on the nanoscale were previously reported.[35,36] Herein, we use this protocol as a unique method to form a hybrid amorphous/crystalline structure. Materials

[a] S. M. B. Khajehbashi, J. Li, M. Wang, Dr. L. Xu, K. Zhao, Dr. Q. Wei, C. Shi, Dr. C. Tang, L. Huang, Z. Wang, Prof. L. Q. Mai
State Key Laboratory of Advanced Technology for Materials Synthesis and Processing
Wuhan University of Technology
Wuhan 430070 (P.R. China)
E-mail: mlq518@whut.edu.cn

[b] Dr. L. Xu
Department of Chemistry and Chemical Biology
Harvard University
Cambridge, MA 02138 (USA)

These are not the final page numbers! ↗↗

in the nanoscale melt at lower temperatures than bulk materials; this concept is known as melting-point depression. The atoms near the surface have lower coordination number and reduced cohesive energy, so by increasing the temperature they can become free from the solid phase easily.[37,38] In this way, by subsequent rapid cooling the surface atoms lose their energy quickly and they can become an amorphous structure in a manner similar to the quenching process in the bulk material. We used this hypothesis to form an amorphous layer on the surface of Co_3O_4 nanoparticles. Upon heating pure cobalt under ambient air conditions to an elevated temperature followed by quenching in air, it is anticipated that the surface atoms will adopt an amorphous structure. In this work, the synergistic behavior of a single crystal and the ultrathin amorphous layer of Co_3O_4 provide the basis of our mechanism for the formation of the hybrid catalyst. With this effective technique, the unaided Co_3O_4 nanoparticles will be considered as a candidate for a high-performance electrocatalyst in the ORR and Li–air batteries. As a new insight, we explain that the origin of the high catalytic performance of the hybrid structures derives from the existence of different active sites in these structures.

Results and Discussion

Catalytic performance in the ORR

Figure 1a shows a schematic process consisting of the synthesis of pure cobalt single crystals, oxidation, and final rapid cooling in air. As mentioned in the Supporting Information, ethylene glycol as both the reducing agent and solvent was employed in the solvothermal method.[39] The X-ray diffraction (XRD) patterns in Figure S1a (Supporting Information) with sharp peaks prove the effective role of ethylene glycol in the synthesis of pure cobalt. The scanning electron microscopy (SEM) image in Figure S1b shows the morphology of a pure cobalt nanoparticle. To optimize the oxidation temperature, we chose four different temperatures, and the samples are named COX200, COX400, COX500, and COX650 for oxidation temperatures of 200, 400, 500, and 650 °C, respectively. The SEM images in Figure S1c–f show a slight coarsening in the morphologies of COX200, COX400, COX500, and COX650 upon increasing the oxidation temperature. Figure 1b shows the XRD patterns of COX200, COX400, COX500, and COX650. Investigation of the XRD patterns in Figure 1b shows a sharp and intense peak for (311) upon increasing the oxidation temperature. All the peaks can be assigned to cubic Co_3O_4 (PDF card No. 00-009-0418). The SEM images and transmission electron microscopy (TEM) images of COX500 as the catalyst candidate are shown in Figure 1c–g. The SEM image in Figure 1c shows the morphology of COX500 agglomerated nanoparticles. The TEM image in Figure 1d shows the general features of the nanoparticles, and the internal pores in the high-resolution TEM (HRTEM) image shown in Figure 1e are clear. These pores provide a suitable pathway for oxygen during the ORR. An amorphous thin layer with a thickness of approxi-

mately 2–3 nm is visible in the high-magnification TEM image shown in Figure 1f. The behavior of the nanomaterials at high temperature, especially including the phase transformation temperature, is not clear. As mentioned before, because of melting-point depression, nanomaterials have lower melting temperatures and the surface atoms have higher mobility because of fewer bonds. In this way, a high cooling rate after heat treatment or oxidation results in the formation of an amorphous layer on the surface of the nanoparticles. In fact, at a high cooling rate, the atoms on the surface do not have enough time to diffuse and adopt their crystalline positions. By considering the liquid shell nucleation (LSN) model, depending on the particle size and cooling rate, an amorphous layer is formed on the particles.[35,37,38,40] Figure 1g shows the (311) crystal planes with d spacing of 0.24 nm, and the selected area electron diffraction (SAED) pattern beside this image is obtained, which proves the single-crystalline structure. We will explain the key role of single crystals in facilitating the ORR and the stability of the Li–air battery during cycling. The reason that COX500 was chosen as a catalyst candidate will be revealed by rotating disc electrode (RDE) and cyclic voltammetry (CV) test results. The RDE and CV tests were performed at scan rates of 5 and 50 mV s^{-1} for each sample, respectively. The potentials in these cases are reported versus the reversible hydrogen potential (RHE), following some reports.[17,41] The CV curves in Figure 2a clearly show that COX500 has the most intense peak of all the samples studied. COX200 and COX400 show quite similar CV behavior, and the performance of COX650 relative to that of COX200 and that of COX400 is just slightly improved. Their onset potentials are low and near the onset potential of Co_3O_4 alone, as reported.[17] The onset potential of COX500 is more positive (0.90 V) than that of Co_3O_4, and the value is higher than that of either Co_3O_4/rmGO (rmGO = reduced mildly oxidized graphene oxide) or N-CG-CoO (N-CG = nitrogen-doped crumpled graphene), as reported.[17,24] The cathodic current of COX500 is markedly higher than those of COX200, COX400, and COX650. As mentioned before, the ORR is known as a sluggish reaction, and the RDE test is a reliable test to measure the kinetics of the ORR. Rotating-disc voltammograms of COX500 are shown in Figure 2b, and the rotating-disc voltammograms of COX200, COX400, and COX650 are shown in Figure S2. From Figure 2b it can be found that the half-wave potential for COX500 is approximately 0.78 V, which is more positive than 0.62 V for COX200, COX400, and COX650 in Figure S2. The linearity of the Koutecky–Levich plots and the near parallelism of the fitting lines suggests first-order reaction kinetics toward the concentration of dissolved oxygen and similar electron-transfer numbers for the ORR at different potentials.[38] The electron-transfer number (n) from the slope of the inset in the Koutecky–Levich plot in Figure 2b was calculated to be approximately 4.0 at 0.20–0.35 V, which is reminiscent of the four-electron oxygen reduction of high-performance catalysts. Actually, our strategy provided a high-performance catalyst with an electron-transfer number of 4.0, which com-

These are not the final page numbers! ↗↗
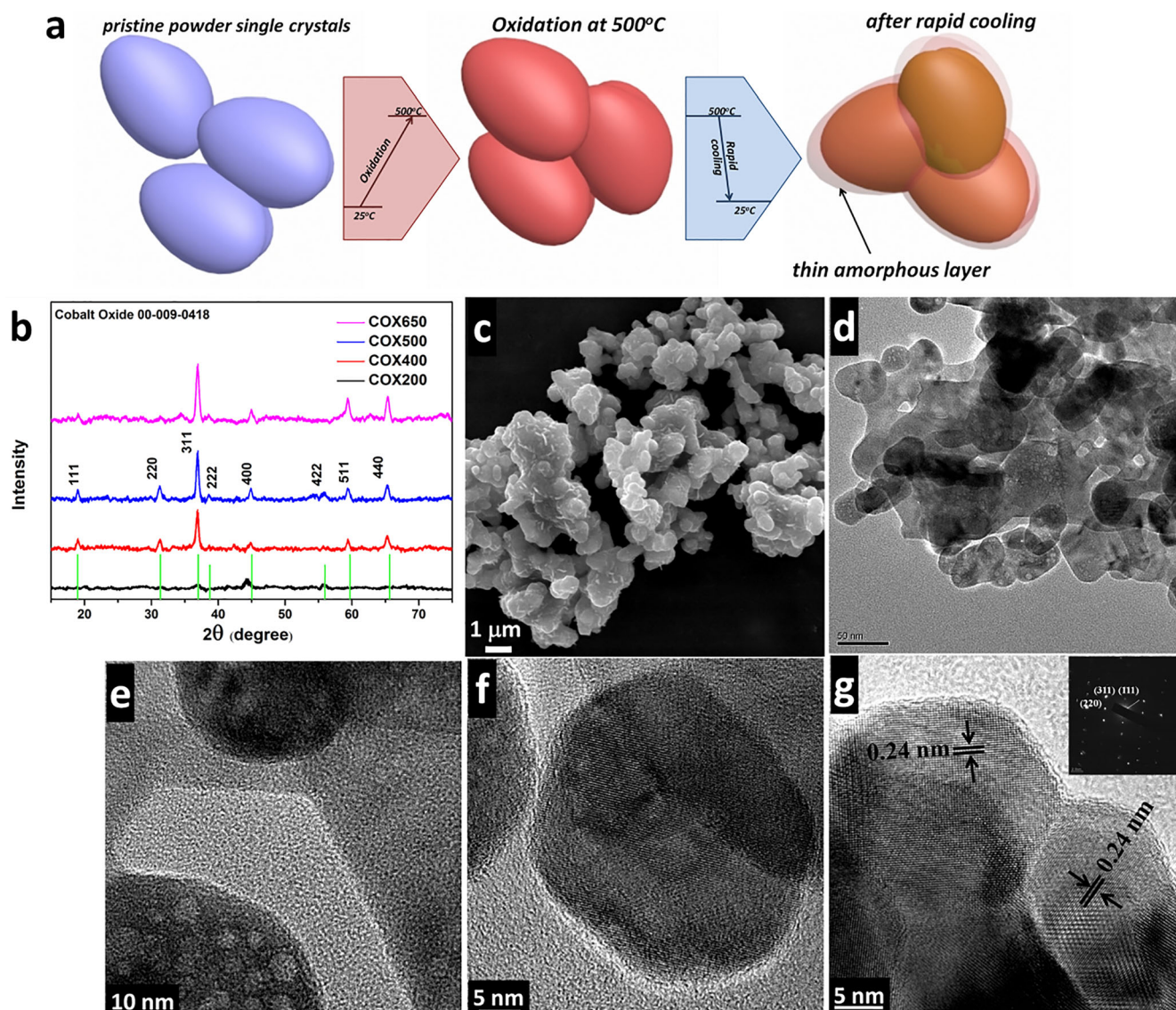
Figure 1. a) Schematic of the oxidation and rapid-cooling process. b) XRD patterns of the four samples with different oxidation temperatures. c) SEM image of COX500 agglomerated nanoparticles. d) TEM image of the general features of COX500 agglomerated nanoparticles. e) HRTEM of COX500 with internal pores. f) High-magnification TEM image of COX500 with an amorphous layer. g) High-magnification features of COX500 single crystals with SAED pattern in the inset.

petes with the Co_3O_4/rmGO or CG/CoO hybrid catalysts.[17,24] Figure 2c shows the RDE graphs of the four samples at a speed of 1600 rpm, which proves the rapid-cooling strategy is optimized at 500 °C. The RDE and CV tests results prove that our strategy is effective in providing a good catalyst candidate for the ORR in the case of COX500. The RDE test results prove that this bare in situ hybrid electrocatalyst has high catalytic performance; however, it still has not reached the performance of Pt/C or some other composite catalysts. In fact, the facile synthesis method and the catalytic performance of this bare catalyst simultaneously show its preferred advantages.

Amorphization and mechanistic investigations

To characterize the effect of the oxidation regime on the formation of the amorphous layer, the samples were investigated by X-ray photoelectron spectroscopy (XPS), and the results are shown in Figure 3. The spectra of cobalt consist of two main peaks and two satellite peaks (Figure 3a). It can be found that for the sample oxidized at 500 °C the main peaks are shifted to lower binding energies relative to the main peaks of the sample oxidized at 200 °C, as the spinel oxides are formed. Upon increasing the oxidizing temperature from 200 to 500 °C, the binding energies of the two main peaks shift from 794.98 to 794.88 eV and from 780.18 to 779.78 eV. To gain more information, the XPS fitting graphs of cobalt for COX200 and COX500 are shown in Figure 3c,d. Comparison of the fitted curves for Co_3O_4 shows that the binding
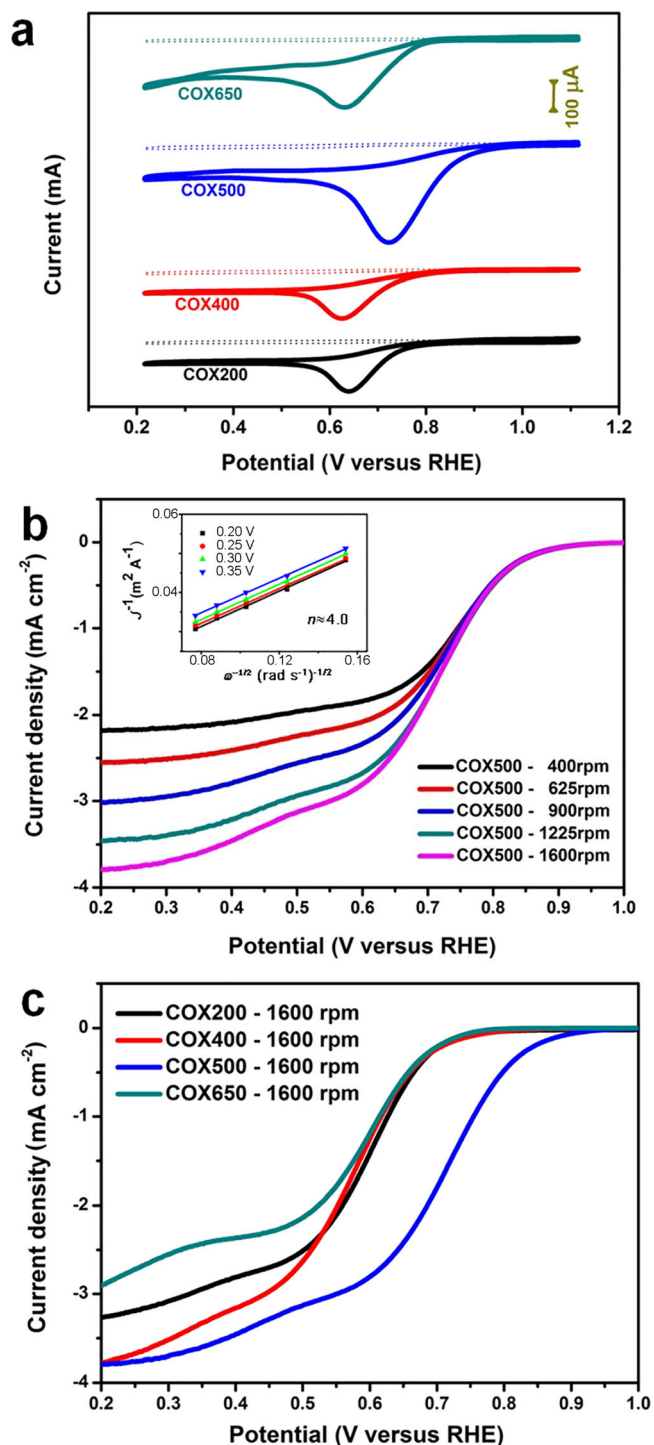
Figure 2. a) CV curves of COX200, COX400, COX500, and COX650 in O$_2$-saturated (——) or Ar-saturated (- - - -) 0.1 M KOH. b) Rotating-disc voltammograms of COX500 (loading ≈0.1 mg cm^{-2}) in O$_2$-saturated 0.1 M KOH and corresponding Koutecky–Levich plots (J^{-1} versus $\omega^{-0.5}$) at different potentials (inset). c) Comparison of the RDE graphs of COX200, COX400, COX500, and COX650 at a speed of 1600 rpm.

energy for COX200 (781.1 eV) is higher than that for COX500 (780.2 eV). As XPS gives surface data for a material, the lower binding energy for cobalt with the same compound is related to the higher coordination number because

of the amorphous surface layer that is found in COX500. Cobalt in Co$_3$O$_4$ has two valance states, Co^{2+} and Co^{3+}. As observed, upon changing the oxidation temperature from 200 to 500 °C, the binding energy shifts to a lower value. In this way, the two bonding types merge toward one bonding type for the amorphous structure in the case of COX500. In addition, the O 1s spectra are shown in Figure 3 b. Here, the O 1s peak has behavior similar to that of the Co 2p3/2 and Co 2p1/2 peaks. The binding energy in this case decreases from 529.98 to 529.88 eV. This decrease can be explained as per the bond merging in the amorphous layer, as reported.[42] According to Figure 3 b, the small shoulder at a binding energy of 531.18 eV is related to the hydroxy group. Comparison of the two spectra in Figure 3 b reveals that the O 1s peak is more intense for the COX500 sample than for the COX200 sample but the peak for the hydroxy group is less intense for COX500 than for COX200, and thus COX500 can be a good candidate for a catalyst in the ORR.

Raman spectroscopy is more powerful than X-ray analysis for detecting and monitoring crystallization/amorphization in some cases.[43] For bulk cobalt, the hexagonal close-packed (HCP) structure is stable below 425 °C, the face-centered cubic (FCC) structure is stable at higher temperatures, and the metastable phase of ε-Co nanocrystals can form in the solution phase, which is not controlled by thermodynamics.[44] We employed Raman spectroscopy to investigate the samples with oxidation regimes higher and lower than this temperature. Figure 3 e shows the Raman spectra of Co$_3$O$_4$ with two different oxidation regimes. According to Figure 3 e, it is clear that COX400 has no intensity increase in the baseline, which is in contrast to that observed for COX500. With the estimation in Figure 3 e (blue graph), the percentage of the graph area that involves the common peaks relative to the whole graph area is approximately 10 %, and the remaining 90 % has no local peaks but has increasing behavior, which makes a shoulder peak. As previously reported,[43] organic amorphous materials, such as amorphous carbons, and inorganic materials, such as silicates, phosphates, niobiates, and titanates, have this type of shoulder peak involving Boson peaks. This similarity suggests that the shoulder section of COX500 is related to the amorphous layer, which is shown in Figure 1 f. Deviation of a Raman spectrum with a flat baseline (COX400) toward a high slope shape baseline (COX500) can be a good criterion to characterize surface amorphization. The common peaks among both samples include three main peaks and two satellite peaks, which match the peaks of crystalline Co$_3$O$_4$, as shown clearly in Figure 3 f.[45] The Raman spectrum of COX500 shows bands that are more intense than those of COX400, and the Raman shift values are lower than those of COX400. The bands of COX500 are clearly broadened relative to those of COX400 (Figure 3 f), which proves disordering in the surface of COX500. In this way, shifting of the Raman spectra to lower values and broadening of the bands evince the amorphous (wide Gaussian band) surface layer in the case of COX500 and a crystalline nature (narrow Lorentzian) in the case of COX400.[43] Comparison of these graphs shows that the
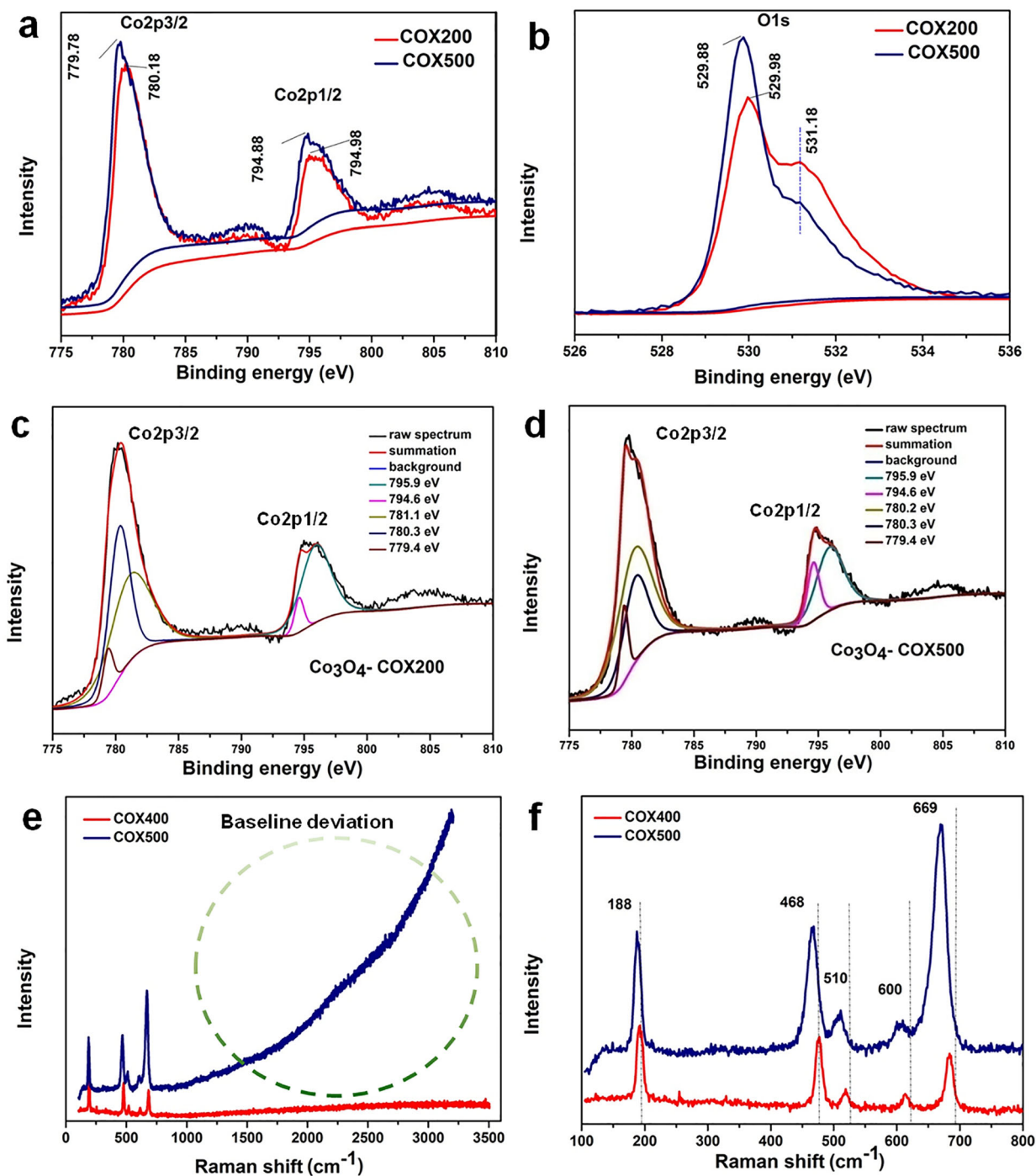
Figure 3. a) Cobalt XPS spectra of COX200 and COX500. b) Oxygen XPS spectra of COX200 and COX500. c) XPS spectra of cobalt with Co_3O_4 fitting curves for COX200. d) XPS spectra of cobalt with Co_3O_4 fitting curves for COX500. e) Comparison of Raman spectra of COX400 and COX500. f) Focusing on bands of the Raman spectra involving the three main peaks and two satellite peaks.

phase-transition temperature of cobalt is critical during oxidation. Our Raman spectroscopy results declare that the total behavior of the Raman spectra over a wide range in addition to band broadening can be a good criterion for amorphization in Co_3O_4.

The TEM images, XPS results, and Raman spectra proved the effective role of rapid-cooling synthesis on the surface amorphization of the Co_3O_4 nanoparticles. In the amorphous

structure, the atoms are available everywhere for reaction, so they provide more probable sites for the ORR, but disordering of these atoms causes many barriers for electron transfer, so the electronic conductivity will decrease. On the another hand, the surface layer participates in the initiation of the ORR and reduces the overpotential by providing low-barrier sites for reaction, and after that the reaction will follow toward the internal pores and between the single crystals. In

These are not the final page numbers! ↗↗

addition, because some residual stress is induced on the surface of the catalyst during the rapid-cooling process, this decreases the energy barrier for initiation of the ORR.

The main problem associated with reducing oxygen is its multiple bonding nature, which makes the bond very strong. In fact, the duty of a catalyst is to weaken this bond to optimize the oxygen-bonding energy, and this is known as Sabatier's principle[46] (see Figure S3). According to this theory, we introduce a mechanism for a hybrid catalyst in the initiation of the ORR. The first step of the mechanism for the ORR is adsorption of oxygen on the catalyst surface.[45] It must first be considered that the oxygen molecules encounter the catalyst surface, and in the case of a catalyst with a whole uniform structure, the entire catalyst surface has the same energy. The uniform surface provides uniform conditions for the oxygen molecules without any effective force on oxygen bonding. If the catalyst has nonuniform surface properties, for example, in a hybrid structure, then according to the "Yeager model" two oxygen atoms in contact with the different sites will have two unequal activities. This difference in activities causes distinctive vibration and movement of the two atoms, and this can result in weakening of the oxygen bond. In other words, one atom of oxygen reduces the surface energy if it is adsorbed on the surface of the catalyst, whereas another atom cannot reduce this energy as much as the first atom, because of the different energy level of the active site. This situation provides more vibration and less rigidity for a second O atom relative to the first atom, which finally causes weakening of the oxygen bond as the favorite site for initiation of the ORR. The mechanism of the hybrid crystalline/amorphous electrocatalyst is schematically illustrated in Figure 4a. In this figure, by considering the dissociative reaction as an example, in the adsorption step, two different active sites have synergistic behavior. As XPS is a surface analysis method, the higher binding energy of the oxygen in COX200 (529.98 eV) relative to that in COX500 (529.88 eV) proves the effect of different coordination numbers in the crystalline and amorphous states. The single-crystalline structure with long-range order and minimum grain boundaries has a lower energy state and provides a lower coordination number around the oxygen atom. In this way, the oxygen atom in the crystalline active site has less mobility than the oxygen atom in the amorphous active site. A combination of single crystals beside the amorphous layer creates more contrast in the active sites, which should result in better performance in the ORR, as we saw in the RDE test results. As mentioned in the Introduction, by combining different materials, hybrid catalysts may show better performance in the ORR than the individual components. In their synthesis processes, the reducing gas such as H_2 or doping gas such as NH_3 has a cooling effect on the material in the tube furnace. So, it should be noted that the surface of the reduced or doped material can be partially amorphized. In some reports, the importance of active sites in the carbon or amorphous structure of CoS_2 as a catalyst in the ORR were mentioned; however, the origin of these active sites or

their synergistic behavior to facilitate the ORR were not discussed.[47–50]

We will show that this catalyst has high performance in Li–air batteries with a non-aqueous electrolyte. It can be seen in Figure 4b that after 50 cycles in the Li–air battery, the planes are displaced relative to those in the pristine sample, and the inset SAED pattern shows stable participation of the planes during charge/discharge. The amorphous layer thickens, as shown in Figure 4c, and the inset SAED pattern in this image is obtained from the amorphous layer. Single-crystal plane displacement and amorphous-layer thickening match with the dynamic mechanism in the hybrid catalyst.

Utilization of the catalyst in Li–air batteries

Examination of the RDE and CV test results alongside the TEM measurements encouraged us to employ COX500 as an electrocatalyst in a Li–air battery. Figure 5 shows the charge/discharge, electrochemical impedance spectroscopy (EIS) curves, and CV curves for the Li–air battery. It is clear in Figure 5a,b that at a current density of $100\,\mathrm{mA\,g^{-1}}$ the cycling is stable with a limited specific capacity of $1000\,\mathrm{mAh\,g^{-1}}$ over as many as 120 cycles ($\approx 2500\,\mathrm{h}$) with 100% efficiency. The average discharge voltage is approximately 2.80 V, which confirms the high catalytic performance of the crystalline/amorphous hybrid catalyst in the Li–air battery. The average charge voltage except for the final cycle is approximately 4.0 V, which is much lower than the charge voltage in the presence of pure carbon (4.5 V) and some other hybrid catalysts.[5,30] Figure S4 shows the potential versus real-time cycling of the Li–air battery, and it proves continuous cycling for approximately 2500 h. In the case of full charge/discharge (Figure S5), the battery reaches a specific capacity higher than $10\,000\,\mathrm{mAh\,g^{-1}}$, and it maintains this high specific capacity until the 10th cycle at a current density of $200\,\mathrm{mA\,g^{-1}}$. The Li–air battery with this catalyst shows better performance and a longer cycling life than many hybrid hierarchical-structured catalysts and noble-metal catalysts.[3,5,11,30] The EIS curves are shown in Figure 5c. The impedance of charge transfer is reversible after charging and can be shifted toward the pristine battery. The curve of specific capacity versus voltage shows two plateaus in the initial cycle, which was illustrated before, and this might be caused by shifting of the ORR from the amorphous layer toward the crystal. CV was performed by cycling the Li–air battery while it was in an oxygen-filled glovebox. The CV curves of the Li–air battery under these conditions is shown in Figure 5d. Distinctive peaks are clear in both the forward and reverse scans over three cycles. The reversible formation and decomposition of Li_2O_2 corresponds to these peaks according to the ORR and OER, respectively. At a current density of $500\,\mathrm{mA\,g^{-1}}$, the Li–air battery surpasses 40 cycles and a limited specific capacity of $800\,\mathrm{mAh\,g^{-1}}$ is achieved (Figure 5e). The discharge potential in this case is approximately 2.65 V, which 150 mV is lower than the discharge potential at a current density of $100\,\mathrm{mA\,g^{-1}}$. Subsequent charge/discharge with

**These are not the final page numbers!** ↗↗
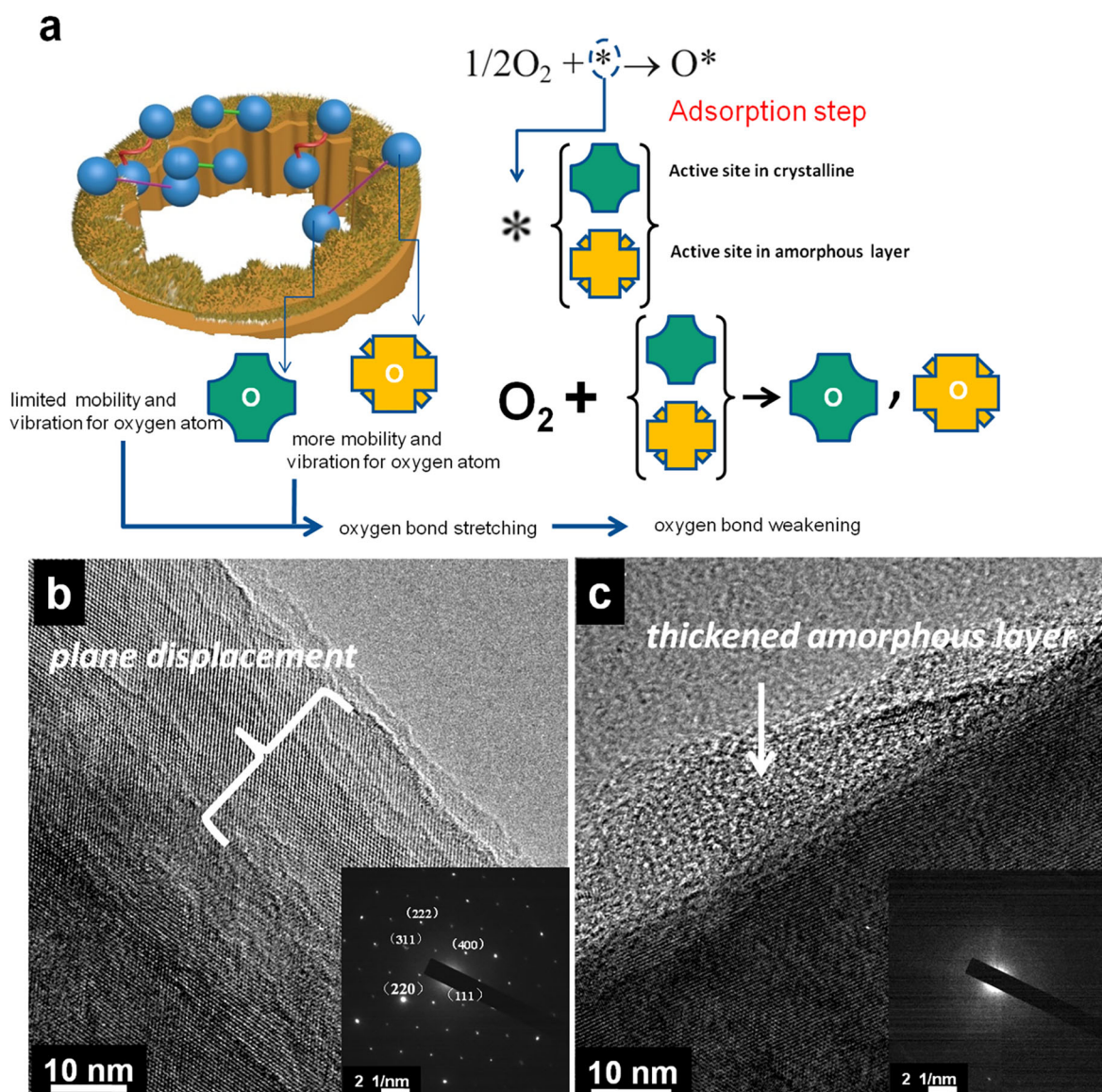
Figure 4. a) Schematic illustration of the mechanism of the hybrid catalyst in the ORR. Synergistic participation of two active sites weakens the oxygen bond. b) HRTEM image of the displaced planes in the crystalline structure of the catalyst after 50 cycles in a Li–air battery with the SAED pattern in the inset. c) Thickened amorphous layer after 50 cycles in the Li–air battery with the SAED pattern of the amorphous layer in the inset.

different current densities (100, 200, 500, and 1000 mA g^{-1}) is shown in Figure 5 f, which shows that upon increasing the current density the discharge potential decreases.

The high catalytic performance of this catalyst in non-aqueous electrolyte was proved by its use in a Li–air battery. To verify the effect of the synthesis process on the formation of the in situ hybrid structure, a witness test was performed. As the rapid-cooling method was optimized at 500 °C for COX500, the characterization and electrochemical performance of a sample with the same oxidation temperature and subsequent slow (normal) cooling was measured. The results of this test are discussed in the Supporting Information. With slow (normal) cooling synthesis, a crystalline/amorphous hybrid structure could not be obtained and the catalyst behavior followed the low performance of common Co$_3$O$_4$ nanoparticles. In fact, the cooling rate and oxidation

temperature together play a key role in obtaining a crystalline/amorphous hybrid catalyst with high catalytic performance.

We also performed charge/discharge measurements of a Li–air battery with the COX500 catalyst under ambient air conditions. As shown in Figure S7 a,b, under these conditions at a current density of 200 mA g^{-1} the Li–air battery sustained five stable cycles with a limited specific capacity of 1000 mAh g^{-1}. Figure S7 c shows a comparison of the fully discharged curves under the oxygen conditions at two different current densities and in air with a current density of 100 mA g^{-1}. Although the cycling performance of the battery in air does not last as long as that under oxygen conditions, it shows a higher specific capacity ($\approx$14000 mAh g^{-1}) in the first fully discharged state at the same current density. This higher specific capacity may be caused by incorporation of

These are not the final page numbers! ⬈⬈
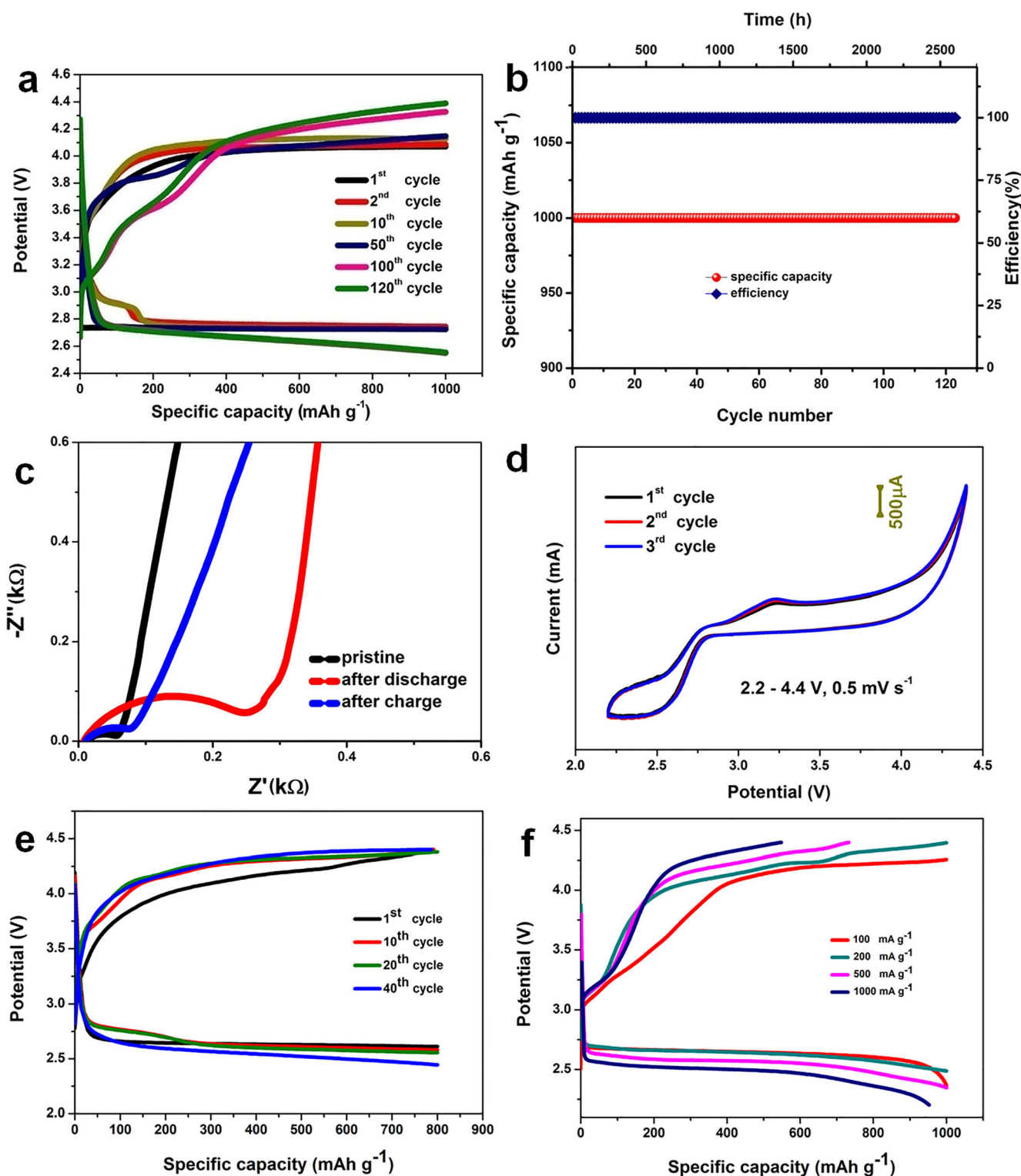
Figure 5. a) Galvanostatic discharge/charge curves of the Li–air battery with a limited specific capacity (1000 mAh g^{-1}) at a current density of 100 mA g^{-1}. b) Cycling performance and capacity retention with a limited specific capacity (1000 mAh g^{-1}) at a current density of 100 mA g^{-1}. c) Electrochemical impedance spectra. d) CV curves of the Li–air battery. e) Discharge/charge curves of the Li–air battery with a limited specific capacity at a current density of 500 mA g^{-1}. f) Subsequent discharge/charge curves of the Li–air battery with a limited specific capacity (1000 mAh g^{-1}) at different current densities.

CO_2 with O_2, as previously reported.[49] The discharge voltage for the battery tested in ambient air decreases to 2.6 V, which is 200 mV lower than the average discharge voltage under the oxygen conditions. It should be considered that in ambient air, H_2O vapor has a disruptive effect and causes some side reactions in the battery.

These are not the final page numbers! ↗↗

To characterize the products of charge/discharge in the Li–air battery, in situ XRD was employed. Figure 6a shows the appearance of Li_2O_2 peaks [$2\theta = 32.9$ and $35.0°$ for (100) and (101), respectively] after 1, 2, and 4 h of discharging. Disappearance of these peaks after full charging is clear in the related XRD pattern. The charge/discharge curves of the Li–air battery for in situ XRD testing is shown in Figure S8. It should be noted that in situ XRD was performed in air, and the moisture in the air could condense on the cell's window, which would disturb the battery reactions and X-ray detection. To restrict this harmful effect, the discharging time was limited to approximately 4 h and a dehumidifier was placed inside the XRD chamber.

As mentioned, moisture and other disturbing gases limited the in situ XRD time. To clarify the discharge products, especially at high-angles region of XRD, ex situ XRD of a Li–air battery fully discharged under oxygen conditions (specific capacity reached $10000\ mAh\,g^{-1}$) was measured. The Li–air battery after fully discharging was disassembled in an oxygen-filled glovebox, and the cathode was removed for ex situ XRD. Distinctive peaks of Li_2O_2 are clear in Figure 6b, and the inset shows the 2D/3D crystal structure of Li_2O_2.[52] It seems that because of complete discharge and the stable testing conditions in the oxygen-filled glovebox with a water content less than 1 ppm, Li_2O_2 was finely crystallized. Figure 6c shows the SEM image of the cathode after full discharge. After full discharge, the surface is covered by large-sized ($\approx 800\ nm$), four-leaf-clover-shaped Li_2O_2. The energy-dispersive X-ray spectrum of the clover-shaped product is shown in the inset of this figure. To the best of our knowledge, this is the first time that this morphology of Li_2O_2 is re-
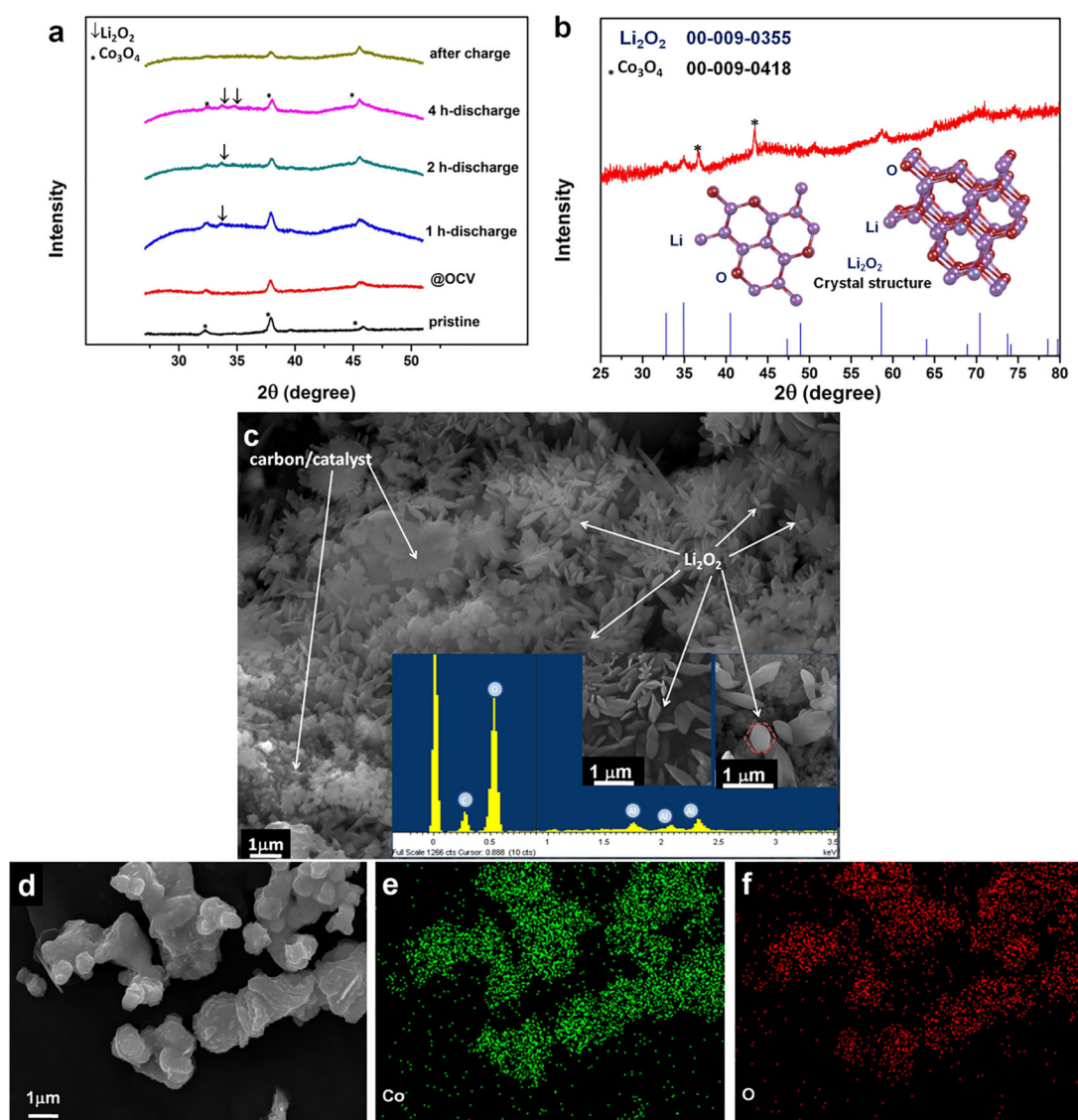
Figure 6. a) In situ XRD pattern of the Li–air battery after 1, 2, and 4 h of discharge and final charge. b) Ex situ XRD pattern of the fully discharged Li–air battery and 2D/3D crystal structure of Li_2O_2 (inset). c) SEM image of the cathode consisting of four-leaf-clover-shaped discharge products after full discharge. The insets show the EDS pattern of the discharge products. d) SEM image of the catalyst particles after 50 cycles. e,f) EDS mapping of the catalyst particles after 50 cycles.

These are not the final page numbers! ↗↗

ported. Further studies are underway to investigate the discharge products of the Li–air battery.

As mentioned in the Introduction, there are many parameters that participate in the ORR/OER of Li–air batteries, and most of the mechanisms are still unclear. Blocking the cathode pores with the ORR product, which is not soluble in non-aqueous electrolytes, has been reported. Christensen et al. illustrated how lithium oxide particles can cause passivation and pore blocking.[53] Upon considering oxygen as an ideal gas and according to the ideal gas law in thermodynamics, during the OER, if the oxide particles trap the oxygen molecules inside the pores, the internal pressure of the pores will increase severely, as calculated in the Supporting Information. On the other hand, upon considering the blocked pores as a closed system, then the localized pressure conditions cause increasing pressure on the OER. According to Le Chatelier's principle, this increased pressure will shift the reaction $(2Li+O_2=Li_2O_2)$ toward the lower molar quantity, and so the lithium peroxide will be more stable. As illustrated in Figure S9, if the mechanical strength of the pore's wall is high enough, then the high localized pressure can provide enough force to break the lithium dioxide particles and the pore will open again. If the mechanical strength of the catalyst's pore wall is low, then the catalyst structure will pulverize. Thus, the mechanical stability of catalyst is critical, and single crystals, because of their high mechanical properties, can be a good choice.

The stability of the COX500 catalyst was investigated after 50 cycles in a Li–air battery. The morphology of the catalyst in the cathode after 50 cycles is shown in Figure 6d. Single crystals of Co_3O_4 preserve their stable structures after 50 cycles, and energy-dispersive X-ray spectroscopy (EDS) mapping of these particles (Figure 6e,f) shows that they consist of cobalt and oxygen (EDS mapping of the cathode after charging is shown in Figure S10). Finally, the key role of the single crystal was revealed. As mentioned in the mechanism for hybrid catalysts, choosing single crystals for greater energy contrast in combination with an amorphous thin layer was intentional. As seen by ex situ SEM, single crystals have high mechanical and chemical stability, which is important for a catalyst in Li–air batteries. High electrical conductivity because of long-range order is another advantage of single crystals, and thus, we recommend the use of single crystals as a catalyst in electrochemical reactions without doubt. In fact, the stability of a Li–air battery relies on the presence of Co_3O_4 single crystals for their surface energy contrast in addition to an amorphous layer to facilitate the ORR and to provide mechanically and chemically stable sites for oxygen and ORR products in the cathode.

Conclusions

We reported a rapid-cooling method as an effective technique for the in situ hybridization of Co_3O_4 nanoparticles. Transmission electron microscopy, X-ray photoelectron spectroscopy, and Raman spectroscopy investigations showed that the strategy of rapid cooling was effective in forming a thin amorphous layer besides a crystalline structure, and this process was optimized at 500 °C. It was found that unaided Co_3O_4 nanoparticles without any supporting material but relying on their in situ hybrid structure provided high catalytic activity for the oxygen reduction reaction (ORR) and Li–air batteries. The rotating disc electrode polarization curves with a half-wave potential of 0.78 V and the cyclic voltammetry curves with an onset potential of 0.90 V proved that the combination of a crystalline/amorphous structure facilitated the ORR. It was verified that the high performance of the hybrid catalyst was provided by a synergistic combination of different active sites. Practically, the use of the unaided Co_3O_4 hybrid catalyst in Li–air batteries with a non-aqueous electrolyte at a current density of 100 mA g^{-1} stabilized the mean discharge voltage at 2.80 V and kept the charge voltage at approximately 4.0 V for 120 cycles. During these 2500 h of continuous cycling, a specific capacity of 1000 mAh g^{-1} with 100 % capacity retention was gained, and in the case of full charge/discharge, a specific capacity of 10000 mAh g^{-1} was achieved. The in situ XRD results showed the appearance/disappearance of Li_2O_2 peaks during charge/discharge, which proved the ORR/oxygen evolution reaction in the Li–air battery. The ex situ X-ray diffraction pattern of the fully discharged Li–air battery proved the hexagonal crystal structure of Li_2O_2 as a discharge product, and a four-leaf-clover morphology of Li_2O_2 was observed for the first time in the scanning electron microscopy image. Ex situ investigations revealed the key role of the single crystals in the stability and high performance of the Li–air battery. This work may open a new window to the synthesis of high-performance electrocatalysts by the rapid-cooling method. As this catalyst is free from precious metals and is not supported with any excess material, production on an industrial scale is reasonable.

Experimental Section

Synthesis of cobalt oxide

The synthesis of Co_3O_4 consisted of two main steps. First, pure cobalt single crystals were synthesized by the solvothermal method, and then the pure cobalt was oxidized in a muffle furnace with subsequent rapid cooling in air. We followed the procedure of Dong et al. with some modifications to synthesize the pure cobalt single crystals.[39] Details of the synthesis of the pure cobalt single crystals is described in the Supporting Information.

Four different heating regimes with the same heating rate (5 °C min^{-1}) were considered for oxidation (2 h at 200 °C, 2 h at 400 °C, 2 h at 500 °C, and 2 h at 650 °C) and then rapid cooling was done in air. Typically, each time approximately 200 mg of powder in an alumina boat was loaded in the muffle furnace. To apply the rapid-cooling conditions, after 2 hours of oxidation in the furnace, the oxidized powder was transferred to a cold alumina crucible and was shaken smoothly. To check the effect of the cooling rate, the same sample after oxidation at 500 °C was cooled in the furnace with a slow cooling rate. The average cooling rates under the rapid-cooling and slow-cooling conditions were measured to be approximately 33.80 and 0.04 °C s^{-1}, respectively.

These are not the final page numbers! ↗↗

Rotating disc electrode test

After the synthesis of each sample, electrochemical measurements were performed in a thermostated standard three-compartment electrochemical cell by using linear potential sweep on rotating disc electrode setup (Pine Instruments) with a bipotentiostat and rotation speed control. ORR activity as a key parameter for catalysts was assessed in 0.1 M KOH solution and the cyclic voltammograms were also measured. Although we used the saturated calomel electrode (SCE), separated by an electrolytic bridge, all potentials were calculated with respect to the measured reversible hydrogen potential (RHE).[17,36,38] RDE test sample preparation and measurements are described in the Supporting Information.

Electrochemical testing of the Li–air battery

Typically, the Co_3O_4 catalyst, super P carbon (SPC), and polyvinylidene fluoride (PVDF) as a binder were selected in a mass ratio of 3:6:1. A mixture of the catalyst and SPC was added to a 10% solution of PVDF and N-methyl-2-pyrrolidone (NMP), which was previously sonicated, and then the mixture was sonicated again for 2 h. The nickel foam current collector was prepared by degreasing in acetone, then putting it in a ethanol and deionized water solution and sonicating for 10 h. After that the nickel foam sheet was rinsed with deionized water extensively and dried in a vacuum oven overnight at 70 °C. Ink was drop casted and spread onto the nickel foam simultaneously (mass of active material loaded was ≈ 0.5–1.0 mg cm^{-2}) Then, the prepared cathode was kept in the vacuum oven to dry at 70 °C overnight. After punching the dried cathode to the desired size, the batteries were assembled with meshed CR2025 coin-cell cases in a glovebox filled with pure oxygen and a water content less than 0.1 ppm. Lithium pellets were used as the counter electrode and lithium bis(trifluoromethanesulfonyl)imide/tetraethylene glycol dimethyl ether (LITFSI/TEGDME) was used as the electrolyte. Galvanostatic charge/discharge was investigated in the potential range of 4.4 to 2.2 V versus Li/Li$^+$ with a multichannel battery testing system (LAND CT 2001A), and the batteries were placed inside an oxygen-filled glovebox with a water content less than 0.1 ppm. In all cases, the specific capacity is reported per mass of the catalyst. Electrochemical impedance spectroscopy was measured with the same testing system in AC impedance mode. CV was measured with the same device in the potential window of 2.2 to 4.4 V and a scan rate of 0.5 mV s^{-1}.

In situ XRD

In situ XRD was employed to characterize the products of the ORR/OER in the Li–air battery. For this purpose, an Advance D8 X-ray diffractometer with a non-monochromated CuK$_\alpha$ X-ray source was employed. The in situ XRD pattern was recorded in the $2\theta = 25.0$–50.0° region. For preparation of the cathode, the catalyst, super P carbon, and polytetrafluoroethylene (PTFE) were mixed in a ratio of 3:6:1. Then, the mixed material was rolled between papers and after punching was kept in a vacuum oven overnight at 70 °C. For assembling the in situ XRD battery, a 2025 coin case with a side window was used. The window was exposed to air, and in this way, the in situ XRD experiments were performed in ambient air. Discharge and charge was performed in the voltage window of 2.2 to 4.2 V with a current density of 200 mA g^{-1}. The time of charge and discharge was limited to approximately 4 h to prevent water condensation on the battery window.

Material characterization

For crystalline structure investigation, and Advance D8 X-ray diffractometer with a non-monochromated CuK$_\alpha$ X-ray source was employed. Morphological study was done with a field-emission scanning electron microscope (JEOL-7100F), a transmission electron microscope, and a high resolution transmission electron microscope (JEM-2100F STEM/EDS) associated with selected area electron diffraction (SAED). Raman spectra were obtained by using a Renishaw IN VIA micro-Raman spectroscopy system, and X-ray photoelectron spectroscopy (XPS) was used for comparison of the binding energies.

[1] H. D. Lim, K. Y. Park, H. Song, E. Y. Jang, H. Gwon, J. Kim, Y. H. Kim, M. D. Lima, R. O. Robles, X. Lepro, R. H. Baughman, K. Kang, *Adv. Mater.* **2013**, *25*, 1348.

[2] A. Kraytsberg, Y. Ein-Eli, *J. Power Sources* **2011**, *196*, 886.

[3] K. S. Kim, Y. J. Park, *Nanoscale Res. Lett.* **2012**, *7*, 47.

[4] K. M. Abraham, Z. A. Jiang, *J. Electrochem. Soc.* **1996**, *143*, 1.

[5] M. M. Ottakam Thotiyl, S. A. Freunberger, Z. Q. Peng, Y. H. Chen, Z. Liu, P. G. Bruce, *Nat. Mater.* **2013**, *12*, 1050.

[6] P. G. Bruce, S. A. Freunberger, L. J. Hardwick, J. M. Tarasco, *Nat. Mater.* **2011**, *11*, 19.

[7] L. Grande, E. Paillard, J. Hassoun, J. B. Park, Y. J. Lee, Y. K. Sun, S. Passerini, B. Scrosati, *Adv. Mater.* **2015**, *27*, 784.

[8] J. Lu, K. Amine, *Energies* **2013**, *6*, 6016.

[9] D. Wittmaier, S. Aisenbrey, N. Wagner, K. A. Friedrich, *Electrochim. Acta* **2014**, *149*, 355.

[10] K. N. Jung, S. M. Hwang, M. S. Park, K. J. Kim, J. G. Kim, S. X. Dou, J. H. Kim, J. W. Lee, *Sci. Rep.* **2015**, *5*, 7665.

[11] X. Lin, Y. Shang, L. Li, A. Yu, *ACS Sustainable Chem. Eng.* **2015**, *3*, 903.

[12] M. Balaish, A. Kraytsberg, Y. Ein-Eli, *Phys. Chem. Chem. Phys.* **2014**, *16*, 2801.

[13] M. A. Rahman, X. Wang, C. A. Wen, *J. Appl. Electrochem.* **2014**, *44*, 5.

[14] J. Lu, L. Li, J. B. Park, Y. K. Sun, F. Wu, K. Amine, *Chem. Rev.* **2014**, *114*, 5611.

[15] Z. Wang, J. Sun, Y. Cheng, C. Niu, *J. Phys. Chem. Lett.* **2014**, *5*, 3919.

[16] Y. C. Lu, H. A. Gasteiger, M. C. Parent, V. Chiloyan, Y. S. Horn, *Electrochem. Solid-State Lett.* **2010**, *13*, A69.

[17] Y. Liang, Y. Li, H. Wang, J. Zhou, J. Wang, T. Regier, H. Dai, *Nat. Mater.* **2011**, *10*, 780.

[18] Y. Liang, H. Wang, P. Diao, W. Chang, G. Hong, Y. Li, M. Gong, L. Xie, J. Zhou, J. Wang, T. Z. Regier, F. Wei, H. Dai, *J. Am. Chem. Soc.* **2012**, *134*, 15849.

[19] T. Zhang, F. Cheng, J. D, Y. Hu, J. Chen, *Adv. Energy Mater.* **2015**, *5*, 1400654.

[20] X. Liu, W. Liu, M. Ko, M. Park, M. G. Kim, P. Oh, S. Chae, S. Park, A. Casimir, G. Wu, J. Cho, *Adv. Funct. Mater.* **2015**, *25*, 5799.

[21] R. R. Mitchell, B. M. Gallant, C. V. Thompsona, Y. S. Horn, *Energy Environ. Sci.* **2011**, *4*, 2952.

[22] E. Yilmaz, C. Yogi, K. Yamanaka, T. Ohta, H. R. Byon, *Nano Lett.* **2013**, *13*, 4679.

[23] C. H. Huang, S. J. Liu, W. S. Hwang, *Energy* **2011**, *36*, 4410.

[24] S. Mao, Z. Wen, T. Huang, Y. Hou, J. Chen, *Energy Environ. Sci.* **2014**, *7*, 609.

[25] P. W. Menezes, A. Indra, N. R. Sahraie, A. Bergmann, P. Strasser, M. Driess, *ChemSusChem* **2015**, *8*, 164.

[26] P. W. Menezes, A. Indra, D. G. Flores, N. R. Sahraie, I. Zaharieva, M. Schwarze, P. Strasser, H. Dau, M. Driess, *ACS Catal.* **2015**, *5*, 2017.

[27] Y. Wang, X. Ma, L. Lu, Y. He, X. Qi, Y. Deng, *Int. J. Hydrogen Energy* **2013**, *38*, 13611.

[28] C. Tran, X. Q. Yang, D. Qu, *J. Power Sources* **2010**, *195*, 2057.

[29] A. K. Thapa, K. Saimen, T. Ishihara, *Electrochem. Solid-State Lett.* **2010**, *13*, A165.

[30] Y. C. Lu, Z. Xu, H. A. Gasteiger, S. Chen, K. H. Schifferli, Y. S. Horn, *J. Am. Chem. Soc.* **2010**, *132*, 12170.

[31] L. Li, S. H. Chai, S. Daib, A. Manthiram, *Energy Environ. Sci.* **2014**, *7*, 2630.

[32] Y. Liang, H. Wang, J. Zhou, Y. Li, J. Wang, T. Regier, H. Dai, *J. Am. Chem. Soc.* **2012**, *134*, 3517.

[33] X. Liua, M. Park, M. G. Kim, S. Gupta, X. Wang, G. Wu, J. Cho, *Nano Energy* **2016**, *20*, 315.

[34] H. Jia, J. Stark, L. Q. Zhou, C. Ling, T. Sekito, Z. Markin, *RSC Adv.* **2012**, *2*, 10874.

[35] Y. Song, L. L. Henry, W. Yang, *Langmuir* **2009**, *25*, 10209.

[36] L. Sun, PhD Thesis, Dept. Mater. Eng., Uni. Wollonggong, **2000**.

[37] G. Schmid, B. Corain, *Eur. J. Inorg. Chem.* **2003**, *2003*, 3081.

[38] *Advances in Nanomaterials* (Eds.: M. Husain, Z. H. Khan), Springer, India, **2016**.

[39] X. Dong, M. Qi, Y. Tong, F. Ye, *Mater. Lett.* **2014**, *128*, 39.

[40] C. Q. Sun, Y. Wang, B. K. Tay, S. Li, H. Huang, Y. B. Zhang, *J. Phys. Chem. B* **2002**, *106*, 10701.

[41] K. J. J. Mayrhofer, D. Strmcnik, B. B. Blizanac, V. Stamenkovic, M. Arenz, N. M. Markovic, *Electrochim. Acta* **2008**, *53*, 3181.

[42] X. Yan, L. Tian, M. He, X. Chen, *Nano Lett.* **2015**, *15*, 6015.

[43] G. Gouadec, P. Colomban, *Prog. Cryst. Growth Charact. Mater.* **2007**, *53*, 1.

[44] V. A. de la Peña O'Shea, I. de P. R. Moreira, A. Roldán, F. Illas, *J. Chem. Phys.* **2010**, *133*, 024701.

[45] V. G. Hadjiev, M. N. Iliev, I. V. Vergilov, *J. Phys. C* **1988**, *21*, L199.

[46] P. Sabatier, *Ber. Dtsch. Chem. Ges.* **1911**, *44*, 1984.

[47] C. Song, J. Zhang, Z. Shi, *PEM Fuel Cell Electrocatalysts and Catalyst Layers: Fundamentals and Applications* (Ed.: J. Zhang), Springer, London, **2008**.

[48] N. Kornienko, J. Resasco, N. Becknell, C. M. Jiang, Y. S. Liu, K. Nie, X. Sun, J. Guo, S. R. Leone, P. G. Yang, *J. Am. Chem. Soc.* **2015**, *137*, 7448.

[49] J. D. Benck, Z. Chen, L. Y. Kuritzky, A. J. Forman, T. F. Jaramillo, *ACS Catal.* **2012**, *2*, 1916.

[50] H. G. S. Casalongue, J. D. Benck, C. Tsai, R. K. B. Karlsson, S. Kaya, M. Ling, L. G. M. Pettersson, F. A. Pedersen, J. K. Norskov, H. Ogasawara, T. F. Jaramillo, A. Nilsson, *J. Phys. Chem. C* **2014**, *118*, 29252.

[51] K. Takechi, T. Shiga, T. Asaoka, *Chem. Commun.* **2011**, *47*, 3463.

[52] F. Fehér, L. von Wilucki, G. Dost, *Chem. Ber.* **1953**, *86*, 1429.

[53] J. Christensen, P. Albertus, R. S. Sanchez-Carrera, T. Lohmann, B. Kozinsky, R. L. J. Ahmed, A. Kojica, *J. Electrochem. Soc.* **2012**, *159*, R1.

These are not the final page numbers! ↗↗

FULL PAPERS

Up in the air: A crystalline/amorphous Co₃O₄ electrocatalyst, synthesized by rapid cooling, is shown to be a promising catalyst for the oxygen reduction reaction. The catalyst is prepared without any aiding material and shows high catalytic performance. This catalyst is stable and has a long cycling life in Li–air batteries. The facile synthesis method and the high catalytic performance are preferred advantages of this catalyst.
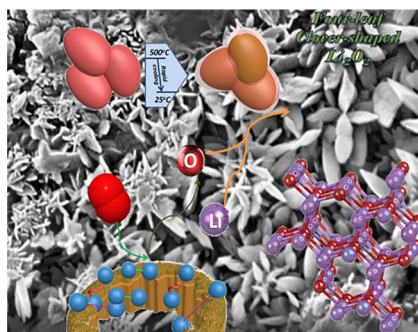
S. M. B. Khajehbashi, J. Li, M. Wang, L. Xu, K. Zhao, Q. Wei, C. Shi, C. Tang, L. Huang, Z. Wang, L. Q. Mai*

■■ – ■■

A Crystalline/Amorphous Cobalt(II,III) Oxide Hybrid Electrocatalyst for Lithium–Air Batteries

These are not the final page numbers! ↗↗